J Seismol
DOI 10.1007/s10950-009-9175-x

ORIGINAL ARTICLE

Occurrence probability of moderate to large earthquakes in Italy based on new geophysical methods

Dario Slejko · Alessandro Caporali · Mark Stirling · Salvatore Barba

Received: 19 March 2008 / Accepted: 16 July 2009
© Springer Science + Business Media B.V. 2009

Abstract We develop new approaches to calculating 30-year probabilities for occurrence of moderate-to-large earthquakes in Italy. Geodetic techniques and finite-element modelling, aimed to reproduce a large amount of neotectonic data using thin-shell finite element, are used to separately calculate the expected seismicity rates inside seismogenic areas (polygons containing mapped faults and/or suspected or modelled faults). Thirty-year earthquake probabilities obtained from the two approaches show similarities in most of Italy: the largest probabilities are found in the southern Apennines, where they reach values between 10% and 20% for earthquakes of $M_W \geq 6.0$, and lower than 10% for events with an $M_W \geq 6.5$.

D. Slejko (✉)
Istituto Nazionale di Oceanografia
e di Geofisica Sperimentale, Sgonico (Trieste), Italy
e-mail: dslejko@ogs.trieste.it

A. Caporali
University of Padua, Padua, Italy
e-mail: alessandro.caporali@unipd.it

M. Stirling
GNS Science, Lower Hutt, New Zealand
e-mail: M.Stirling@gns.cri.nz

S. Barba
Istituto Nazionale di Geofisica e Vulcanologia,
Rome, Italy
e-mail: barba@ingr.it

Keywords Seismic hazard · Strong earthquakes · Probability · Italy

1 Introduction

Plate tectonics processes produce deformation within the crust of the Earth, and the measurement of such surface deformation is an important boundary condition constraint on the interaction of crustal blocks through time. The distribution in space and time of geodetically derived strain rate will correlate, to some degree, with the geometry and activity of the underlying seismogenic sources, as well as with aseismic processes. In this context, many studies around the world have used geodetic strain rates to estimate earthquake recurrence and probability, providing a valuable supplement or alternative to parameters derived from geologic and seismic catalogue data.

During the period spring 2005 to summer 2007 the Department of the Italian Civil Protection funded several seismological and volcanological projects. One of the seismological projects was entitled "Assessing the seismogenic potential and the probability of strong earthquakes in Italy" (designated S2) and its main goals were: (1) to identify of the seismic sources capable of generating destructive earthquakes (i.e. events with a magnitude larger than 5.5) and (2) to assess the occurrence probability of these events for the

Published online: 25 August 2009

sources. The S2 project was organized in four tasks, and Task 4 was dedicated to the actual computation of the occurrence probabilities. One of the goals was to assess the occurrence probability of strong earthquakes using seismological information, and to calibrate the results with geodetic data. Our working hypothesis is that large earthquakes occur along major faults according to the characteristic earthquake model (Schwartz and Coppersmith 1984). According to this hypothesis, faults show a tendency to generate earthquakes of similar characteristics (magnitude, slip, rupture length, etc.). While considered overly simplistic by the Italian research community, the characteristic earthquake model is useful as a basis for the broad data-based and methodological comparisons made in this study.

Our efforts are strongly motivated by the need to find ways to augment the incomplete coverage of fault mapping in Italy to date. While the fault data set is considered to be 95% complete in the southern Apennines, it is at best only 70% complete in the rest of the country, and 50% complete or less in the offshore (Valensise, personal communication).

Considerable international literature is available regarding the evaluation of the occurrence probability of strong earthquakes on well-defined faults (e.g. WGCEP 2003) and the assessment of time-independent (e.g.: Frankel et al. 2000) and time-dependent seismic hazard [California: 2007 WGCEP (2008), Italy: Peruzza (2006)]. However, two main problems thwart these efforts in Italy: (1) the knowledge of the seismogenic faults in Italy is incomplete in terms of the number of faults and their geometric and seismic characteristics and (2) constraints from geodetic data are problematic because the number of permanent global positioning satellite (GPS) stations in Italy is small, the fact that they have only been in operation a short time interval (about 5 years), and the campaign measurements provide velocities with a large associated uncertainty. Not surprisingly, areal seismogenic sources were defined for areas suspected to contain fault sources as yet unmapped in the Database of the Italian Seismogenic Sources [see Basili et al. (2008) for details]. In the S2 project, these seismogenic areas were used to estimate earthquake recurrence parameters from geodetically measured strain rates. Specifically, the geodetic strain rate would be converted into seismic moment rate ($M_0 R$) and then used to give an upper limit to the seismic potential of the seismogenic sources. Critical to this approach would be the assessment of $M_0 R$ from GPS data, the association of this $M_0 R$ to a geographical area, and the exact definition of a seismogenic source within the geographical area.

Our paper summarizes work undertaken thus far in the framework of the S2 project for the assessment of the occurrence probability in 30 years of moderate-to-large earthquakes within seismogenic areas defined in the Database of the Italian Seismogenic Sources. We develop estimates of $M_0 R$ from: (1) observations from permanent GPS stations (geodetic constraint) and (2) from a 3D geophysical model that incorporates state-of-the-art knowledge on faults, and rheology, and is calibrated from GPS observations [geophysical constraint: Barba (2007)].

2 Basic ideas

Two types of seismogenic sources are defined in the Database of the Italian Seismogenic Sources (Fig. 1). These are mapped faults and seismogenic areas. The mapped faults are generally well constrained from geological and geophysical data, in that a complete geometric and seismic parameterization (length, dip, slip rate, slip-per-event, etc.) are available, along with an evaluation of the uncertainties associated with the source parameters.

Seismogenic areas do not contain mapped faults, but are assumed to produce earthquakes of magnitude 5.5 or greater based on other geological, geomorphological, and geophysical data. Features such as linear valleys along strike from the mapped faults are assumed to be fault controlled, but the lack of field mapping prevents the definition of fault sources at the present time. For the seismogenic areas, the polygon defining the overall source is given in the Database of the Italian Seismogenic Sources, along with the associated parameters (depth, strike, dip, rake,

Fig. 1 Seismogenic areas (*red*) and mapped faults (*yellow*) in the Database of the Italian Seismogenic Sources [modified from Basili et al. (2008)]

and slip rate, expected maximum magnitude) and uncertainty bounds.

The research documented here is aimed at defining the seismic potential of the seismogenic areas from the present strain rate in Italy and in consideration of regional seismicity patterns. As not all the existing faults in the seismogenic areas are known, a statistical procedure was designed (Stirling et al. 2007) to fill the empty space of the seismogenic areas with modelled faults of rupture lengths similar to those of the known fault sources.

The working hypotheses of the present study are as follows:

1. the regional geodetic strain is proportional to the seismic potential of the region (i.e. strain is released by earthquakes and aseismic creep);
2. the earthquakes occur on a pre-defined set of faults (a combination of mapped faults and modelled faults: the total number of faults in each seismogenic area is given by the sum of the mapped and modelled faults);
3. faults produce earthquakes according to the characteristic earthquake model (i.e. a tendency to produce a narrow range of earthquakes at or near the maximum size possible from physical constraints such as fault length) and the total regional $M_0 R$ is released as the sum of characteristic earthquakes;
4. the general magnitude–frequency distribution of a region is described by the Gutenberg–Richter behavior, i.e. at the regional scale, the frequencies of the characteristic earthquakes form a Gutenberg–Richter distribution whose b value is in agreement with the regional b value, obtained by the past seismicity.

According to the above hypotheses, we assume that in the long-term (10^4–10^6 years) the majority of regional seismic release (proportional to the regional geodetic strain) will occur on the mapped or modelled faults, each acting according to the characteristic earthquake model and all together representing a Gutenberg–Richter behavior.

3 The data

The network of some 160 permanent GPS stations has been in operation for a decade (1995–2005) and as part of the European Permanent Network of EUREF and the CERGOP 2 Project of the European Union. Additional local densification stations provide a valuable contribution to the estimate of the average surface strain rate. The strain rate budget for central Europe, determined from GPS observations, is of the order of 20–40 nanostrain per year in a circular area of 150–200-km radius of the eastern Alps (see Fig. 2 where a 100-km ray is shown), corresponding to a velocity range of a few millimeters/year over distances of some hundreds of kilometers (Caporali et al. 2008).

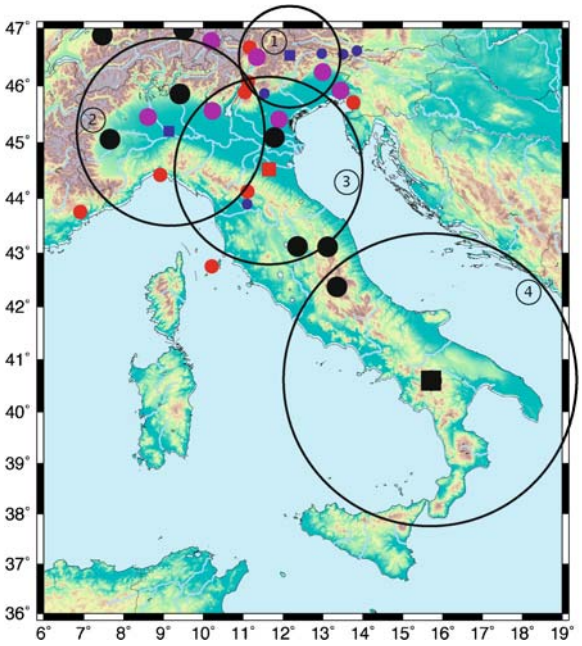

Fig. 2 M_0R (in N·m/year) computed from GPS observations. *Blue small dots* for $M_0R < 1.0 \times 10^{18}$; *red medium dots* $1.0 \times 10^{18} \leq M_0R < 2.0 \times 10^{18}$; *purple medium circles* $2.0 \times 10^{18} \leq M_0R < 3.0 \times 10^{18}$; *black large circles* $M_0R \geq 3.0 \times 10^{18}$. The central GPS station of each domain is marked by a *square* with *size* and *color* according to its M_0R. The *numbered large circles* identify the four domains: *1* eastern Alps, *2* western Alps, *3* central Apennines, *4* southern Apennines

We compute velocity gradients by least squares co-location, which is a minimum variance algorithm capable of rigorously taking into account the stochastic properties of the input velocities (Caporali et al. 2003). For this purpose a covariance function is needed in order to represent the fall off of the correlation coefficient with the lag distance (average distance between the stations). Once the covariance function has been assigned then the velocity and the associated uncertainties can be computed at any point. For deformation analyses it is crucial to know how velocity changes spatially. The horizontal velocity gradient can be split into a symmetric and an anti-symmetric part. The symmetric part represents strain rate, whereas the anti-symmetric part represents a rigid rotation and is, hence, ignorable for deformation studies as the rigid rotation has no associated deformation. The symmetric part can eventually be diagonalized, yielding eigenvectors or principal directions of strain rate. The uncertainty in the components of the strain rate tensor can be quantified from the formal uncertainties of velocities at the actual stations. A final question relates to the method used to compute the strain rates. There exist two schools of thought. One school computes the strain rate on a regular grid, and propagates the uncertainty to account for the loss of accuracy as one moves away from the data points. The other school is more conservative, in the sense that the strain rates are computed only at those points where the estimates are sufficiently well constrained (i.e. where a significant number of stations are close to the site of interest). Hence the strain rate map is patchy, but well constrained where the calculations are made. We adopt this latter approach in our analysis. Specifically, we compute the strain rates at the location of those stations which are surrounded by four or more stations with known velocity within a search radius comparable to the decorrelation distance, that is, the distance at which the average correlation of horizontal velocity pairs drops of 50%.

The horizontal velocities at the GPS stations (see Table 1) are inverted into maximum geodetic strain rate using a search radius variable from 100 to 300 km, according to the number of stations

Table 1 Strain rate (ε') and moment rate (M_0R1), both with related standard deviations, calculated for the GPS stations

STA	Lon. E	Lat. N	Radius (km)	ε' (ns/year)	$\sigma\,\varepsilon'$ (ns/year)	M_0R1 (N·m/year · 10^{18})	$\sigma\,M_0R1$ (N·m/year · 10^{18})
ACOM	13.51	46.55	100	1.73	7.50	0.033	0.141
AFAL	12.17	46.53	100	29.99	6.39	0.565	0.120
AQUI	13.35	42.37	300	31.25	0.25	5.299	0.042
ARDE	10.20	46.78	200	32.88	9.10	2.478	0.686
ASIA	11.53	45.87	200	6.88	1.64	0.518	0.124
BRAS	11.11	44.12	200	17.05	0.33	1.285	0.025
BRIX	10.23	45.56	200	35.90	2.16	2.705	0.163
BZRG	11.34	46.50	100	112.73	4.32	2.124	0.081
CAME	13.12	43.11	300	36.68	3.06	6.219	0.519
ELBA	10.21	42.75	300	8.97	2.00	1.521	0.339
GENO	8.92	44.42	200	22.57	0.18	1.701	0.014
GRAS	6.92	43.75	300	8.28	0.07	1.404	0.012
LEC1	9.41	45.86	200	49.63	6.22	3.740	0.469
MDEA	13.44	45.92	200	29.31	0.87	2.209	0.066
MEDI	11.65	44.52	200	26.30	0.84	1.982	0.063
MERA	11.16	46.67	100	66.98	1.05	1.262	0.020
MPRA	12.99	46.24	200	27.65	3.27	2.084	0.246
NOVA	8.61	45.45	200	37.21	3.34	2.804	0.252
PADO	11.90	45.41	200	31.58	4.56	2.380	0.344
PAVI	9.14	45.20	200	8.24	3.28	0.621	0.247
PRAT	11.10	43.89	200	10.69	1.13	0.806	0.085
ROVE	11.04	45.89	200	18.09	0.46	1.363	0.035
ROVI	11.78	45.09	200	44.33	7.14	3.341	0.538
SARG	9.51	46.98	200	101.92	2.79	7.681	0.210
TITO	15.72	40.60	300	45.24	1.91	7.671	0.324
TORI	7.66	45.06	300	34.56	2.14	5.860	0.363
TREN	11.12	46.07	200	18.69	0.13	1.408	0.010
TRIE	13.76	45.71	200	17.44	2.95	1.314	0.222
UNPG	12.36	43.12	300	31.95	0.51	5.417	0.086
VLCH	13.85	46.61	100	8.12	9.18	0.153	0.173
ZIMM	7.47	46.88	300	33.26	6.63	5.640	1.124
ZOUF	12.97	46.56	200	3.38	1.60	0.255	0.121

available in the circle. More precisely, five seismic domains are considered: eastern Alps, western Alps, northern Apennines, central Apennines, and southern Apennines (Figs. 2 and 3). A 100-km search radius was applied in the eastern Alps, a 200-km radius in the western Alps and northern Apennines, and a 300-km radius in the rest of Italy. This approach is based on that applied by Ward (2007) in California. The maximum geodetic strain rate was translated into geodetic M_0R at the same station locations by the application of the Kostrov's (1974) formula, considering the volume to which that strain rate is related. This passage from strain rate to M_0R is not trivial. In fact, the mean strain rate ε' is equal to the sum of the moment (M_0) tensors of all earthquakes occurring per unit time t in a unit volume V [$V = AH$, where A is the area and H is the seismogenic thickness; Kostrov (1974)], and is given by:

$$\dot{\varepsilon} = \frac{\sum M_0}{2\mu V \Delta t} \tag{1}$$

in which μ is the shear modulus. The crustal volume is obviously a crucial parameter. In our case, the average surface geodetic strain rate is computed considering a circle of 100- to 300-km radius and, consequently, it is assumed to represent the volumetric strain for the seismogenic zone beneath that circle. Equation 1 should define the

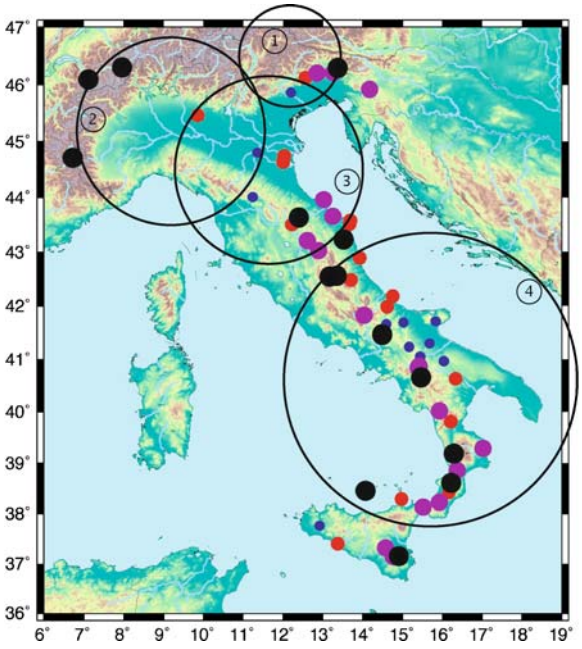

Fig. 3 M_0R (in N·m/year) computed by geophysical modelling for the seismogenic areas. *Blue small dots* for $M_0R < 5.0 \times 10^{15}$; *red medium dots* $5.0 \times 10^{15} \leq M_0R < 1.0 \times 10^{16}$; *purple medium circles* $1.0 \times 10^{16} \leq M_0R < 3.0 \times 10^{16}$; *black large circles* $M_0R \geq 3.0 \times 10^{16}$. The *numbered large circles* identify the four domains: *1* eastern Alps, *2* western Alps, *3* central Apennines, *4* southern Apennines

surface strain rate which can be accommodated in earthquake production in the volume V. A similar definition of the strain volume was already applied by Ward (1994, 1998) and Savage and Simpson (1997), although these authors considered the area to be limited strictly by the GPS stations, while our circles are slightly larger. We adopt an average value of 10 km for the seismogenic thickness because the majority of earthquakes in Italy do not exceed this depth. A shear modulus of 3.5×10^{10} N/m^2 is also adopted. The resulting estimates of regional M_0R from GPS geodesy show a considerable range across the different stations within a given domain (see Fig. 2); for example, in the eastern Alps the M_0R of different stations varies between 0.03×10^{18} and 2.12×10^{18} N·m/year. The M_0R of the central station in each domain was chosen as the M_0R of the whole domain (see Table 2).

Considering the approximations and uncertainties introduced in the method above, we use an additional data set in our analyses. This second data set comes from finite-element modelling conducted to address the misfits between model predictions and a large amount of neotectonic data for Italy (Barba 2007; Barba et al. 2008, 2009). In these studies, model predictions were compared to three independent data sets: geodetic horizontal velocities from temporary and permanent GPS stations (Serpelloni et al. 2002, 2007; Caporali 2007); stress regime data, based on relative stress magnitudes, and the directions of maximum horizontal compressive stress (Montone et al. 2004). The model incorporates faults and realistic rheology in a two-layer grid (crust and lithospheric mantle) with laterally varying seismogenic thickness, heat flow, and topography. The horizontal components of the momentum equation (Kong and Bird 1995) were solved to predict long-term horizontal velocities, anelastic strain rates, verti-

Table 2 M_0Rs of the domains

Domain	Reference station	Search ray (km)	SAN1	M_0R1 (N·m/year)	SAN2	M_0R2 (N·m/year)
E Alps	AFAL-Faloria	100	10	0.56×10^{18}	5	1.01×10^{17}
W Alps	PAVI-Pavia	200	20	0.62×10^{18}	4	1.53×10^{17}
N Apennines	MEDI-Medicina	200	47	1.98×10^{18}	18	3.29×10^{17}
S Apennines	TITO-Tito	300	34	7.67×10^{18}	26	4.77×10^{17}

The index 1 refers to the GPS observations, while the index 2 refers to the results of the geophysical modelling. M_0R1 is computed for the reference station while M_0R2 is given by the sum of the M_0Rs calculated by modelling for the seismogenic areas belonging to each domain. SAN1 represents the number of seismogenic areas inside the search circle and can be larger than the actual number of seismogenic areas inside the domain (the same seismogenic area can belong to more than one domain if it is located in the overlapping areas of search circles). SAN2 is the number of seismogenic areas inside the domain for which M_0R was possible to compute by the geophysical modelling (no overlapping areas as the seismogenic areas are associated to the pertinent domain only)

cally integrated stresses, and fault slip rates. Seismogenic areas were simplistically represented as a single fault trace in these prior studies. In our analysis, we compute the strain and slip rates on the model grid and transform them into M_0R for the different seismogenic areas considering

Table 3 Strain rate (ε') and moment rate (M_0R2), modelled for the seismogenic areas

Source	Region	Lon. E	Lat. N	ε' (ns/year)	M_0R2 (N·m/year · 10^{15})
ITSA002	Cent. South. Alps	9.859	45.460	0.90	6.554
ITSA003	Ripabottoni	15.029	41.685	1.60	1.544
ITSA004	Ascoli Satriano	15.677	41.309	1.40	2.450
ITSA005	Picerno-Massafra	16.328	40.634	21.40	7.068
ITSA006	Sciacca-Gela	13.374	37.407	4.00	5.314
ITSA008	Conero onshore	13.668	43.506	7.80	6.391
ITSA010	Copparo-Comacchio	12.035	44.743	5.90	7.420
ITSA012	Portomaggiore	12.001	44.629	5.40	7.486
ITSA013	Aremogna	14.037	41.822	30.60	16.483
ITSA014	South. Tyrrhenian	14.072	38.460	6.90	53.857
ITSA015	Crati Valley	16.285	39.186	45.20	55.998
ITSA016	Aspromonte	15.516	38.133	118.90	16.699
ITSA017	Scicli-Catania	14.908	37.161	57.90	79.656
ITSA019	Crotone-Rossano	17.022	39.287	14.60	11.859
ITSA020	Southern Marche	13.523	43.229	13.50	46.704
ITSA021	Marsala-Belice	12.921	37.764	5.30	2.142
ITSA024	Castelpetroso	14.487	41.468	51.30	60.454
ITSA025	In. C. Apennines	13.166	42.543	29.10	49.059
ITSA027	Out. C. Apennines	12.401	43.630	12.50	30.959
ITSA028	Colfiorito	12.889	43.024	81.60	15.391
ITSA029	Gela-Catania	14.577	37.324	63.60	28.045
ITSA031	Conero offshore	13.687	43.578	7.50	8.296
ITSA032	Pesaro-Senigallia	13.251	43.650	4.00	18.134
ITSA033	Mt. Pollino South	16.215	39.809	22.40	8.153
ITSA034	Irpinia	15.464	40.663	37.40	54.261
ITSA035	Ragusa-Palagonia	14.766	37.151	13.90	18.460
ITSA037	Mugello	11.237	44.004	23.60	4.128
ITSA038	Mercure Basin	15.929	40.015	39.70	25.133
ITSA040	Castelluccio	13.350	42.561	28.40	57.716
ITSA041	Selci Lama	12.226	43.502	37.60	8.261
ITSA042	Patti-Eolie	14.974	38.298	30.40	9.523
ITSA043	Pesaro-Senigallia	13.019	43.955	7.00	10.580
ITSA051	Mirandola	11.354	44.801	3.10	4.685
ITSA053	Southern Calabria	16.220	38.616	79.70	37.045
ITSA054	Porto San Giorgio	13.924	42.889	13.70	8.434
ITSA055	Bagnara	15.928	38.233	15.70	15.197
ITSA056	Gubbio Basin	12.611	43.210	59.40	23.835
ITSA057	Pago Veiano	15.163	41.238	7.30	2.808
ITSA058	Mattinata	15.830	41.710	1.30	0.969
ITSA059	Tremiti	14.757	42.180	2.20	5.313
ITSA060	Montello	12.202	45.864	15.90	4.273
ITSA061	Cansiglio	12.558	46.117	16.20	8.883
ITSA062	Maniago-Sequals	12.850	46.202	14.60	25.187
ITSA063	Andretta-Filano	15.415	40.874	49.10	26.406
ITSA064	Tramonti-Kobarid	13.378	46.294	11.70	33.937
ITSA066	Gemona-Tarcento	13.265	46.210	28.20	19.751
ITSA068	Catanzaro Trough	16.365	38.861	30.22	24.122
ITSA075	Pietracamela	13.704	42.487	9.50	5.804

Table 3 (continued)

Source	Region	Lon. E	Lat. N	ε' (ns/year)	M_0R2 (N·m/year · 10^{15})
ITSA077	Pescolanciano	14.594	41.654	52.10	2.968
ITSA079	Campomarino	14.612	41.986	4.30	6.424
ITSA080	Nicotera	16.162	38.431	45.00	6.407
ITSA084	Vallata	15.442	41.058	11.50	3.155
ITSA087	Conza -Tolve	15.393	40.840	67.10	22.212
ITSA089	Melfi-Spinazzola	16.036	40.969	1.70	0.972
SISA002	Tolmin-Idrija	14.176	45.918	29.70	15.373

the volume represented by the length, width, and thickness of crust represented by the seismogenic area. A combination of fault slip rate data (where available) and strain rate collectively accounts for known as well as unknown faults (see Table 3). Figure 3 shows the M_0Rs obtained for the seismogenic areas. We note that the transformation of strain rate into M_0R by Eq. 1 is simplistic in the sense that it ignores the possibility that some of the geophysical strain rate may be released aseismically. We consider this issue specifically later in the paper.

Table 2 gives details about the M_0Rs in the domains. The index 1 of the table refers to the GPS observations, while the index 2 refers to the results of the geophysical modelling. In the case of the geodetic constraint, the domain M_0R(M_0R1 in Table 2) corresponds to that calculated for the central GPS station and represents the sum of the M_0R of each seismogenic area in the domain, plus the M_0R of the distributed seismicity (earthquakes of M_W less than 5.5 and, consequently, outside the seismogenic areas), plus that released as aseismic creep. In the case of the geophysical constraint, the domain M_0R(M_0R2 in Table 2) is given by the sum of the M_0Rs of the seismogenic areas calculated by the geophysical modelling. In the case of the geodetic constraint, the number of seismogenic areas inside the search circle (SAN1 in Table 2) can be larger than the actual number of seismogenic areas inside the domain because the same seismogenic area can belong to more than one domain if it is located in the overlapping areas of search circles. As it was not possible to compute the M_0R by the geophysical modelling for all the seismogenic areas, the number of seismogenic areas inside a domain in the case of the geophysical constraint (SAN2 in Table 2) can be less than the actual number of seismogenic areas inside that domain defined in the Database of the Italian Seismogenic Sources. This explains the differences between the numbers in Table 2 and what shown by Figs. 2 and 3.

Figure 2 displays the M_0Rs calculated for the GPS stations from the geodetic observations (circles): the squares highlight the reference stations, whose M_0Rs are associated to the domain (M_0R1 in Table 2) and used as input data in the following computations. The circles in Fig. 3 quantify the M_0R computed by the geophysical modelling for each seismogenic area: the sum of the M_0Rs inside each domain gives the value reported in Table 2 (M_0R2). A direct comparison between the M_0R estimates obtained with the two different methods is not possible. In fact, according to the geodetic constraints, the value reported in Table 2 overestimates the M_0R of the domain because some seismogenic areas are counted more than once as they appear in several domains, depending on the overlapping of the search radii. According to the geophysical constraints, the value reported in Table 2 underestimates the M_0R of the domain because it is not possible to compute the strain rate (and, consequently, the M_0R) for all the seismogenic areas by the geophysical modelling. The two estimates differ by a factor from 5 to 12, and those calculated with geodetic constraints are higher than those computed by the geophysical modelling (see Table 2). This discrepancy is motivated by the fact that the M_0R in each domain from GPS observations is given by the sum of the M_0R released as characteristic earthquakes plus that released as distributed seismicity and as aseismic creep, while the M_0R from geophysical modelling refers only to the contribution of the characteristic earthquakes.

4 Comparison of moment rate derived from geodetic and seismicity data

To compare the observed geodetic moment rate (M_0R1) with the seismic one, domain catalogues have been extracted from the Italian earthquake catalogue (Gruppo di lavoro CPTI 2004). These catalogues collect all the events in a circle centered on the reference GPS stations (Faloria, Pavia, Medicina, and Tito) and with the same radius as that used for the computation of M_0R1: 100 km for Faloria, 200 km for Pavia and Medicina, and 300 km for Tito. The observed seismic moment rate (M_0R_{oss}) in each of the four domains has been computed considering all the earthquakes which have occurred since the beginning of the eighteenth century, because this period can be considered complete for M_W 5.5 and

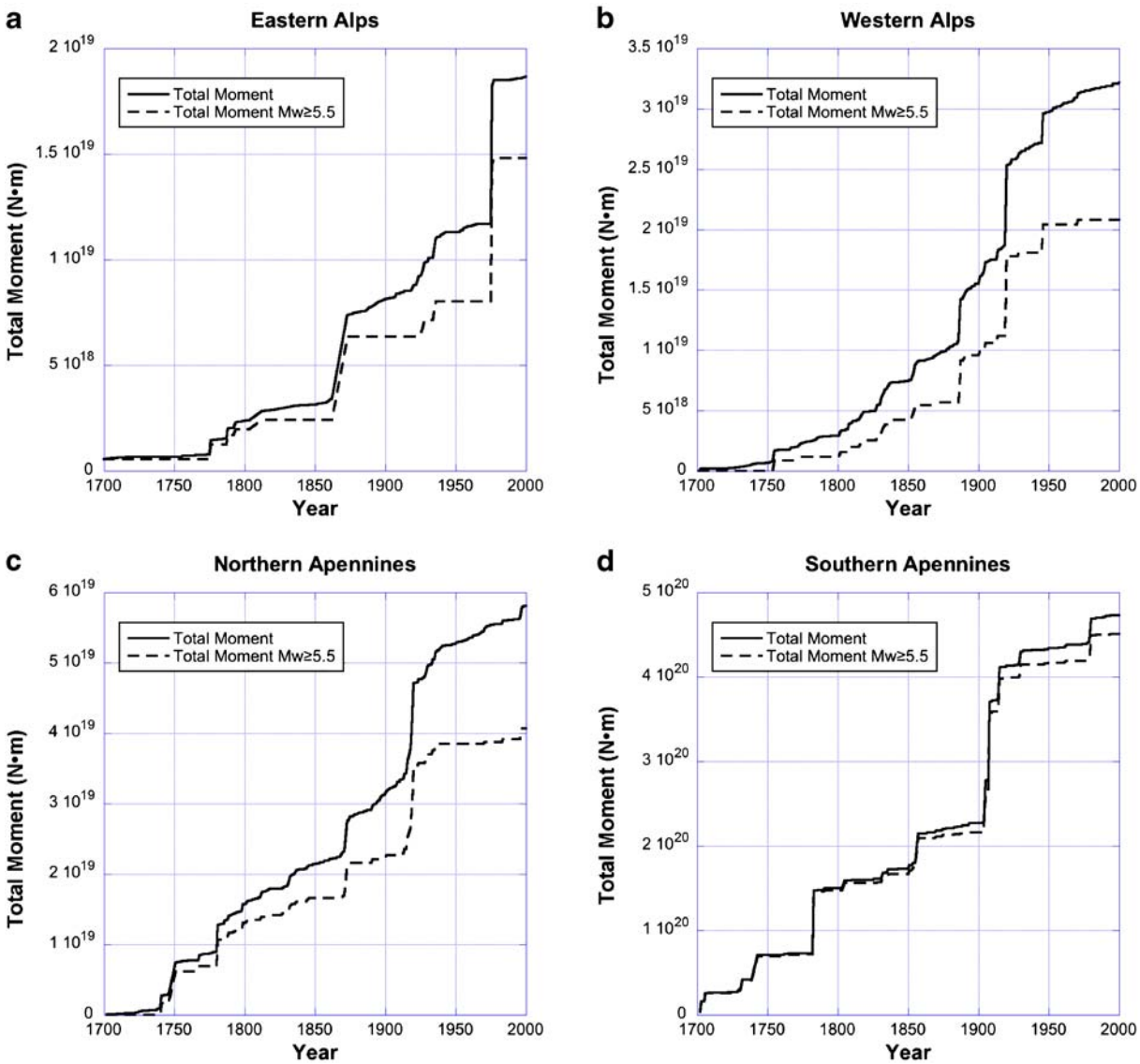

Fig. 4 M_0 release since 1700 in the four domains: **a** eastern Alps, **b** western Alps, **c** northern Apennines, **d** southern Apennines. *Solid line* for all earthquakes of the Italian earthquake catalogue (Gruppo di lavoro CPTI 2004), *dashed line* for events with an M_W 5.5 and over. The *vertical scale* varies in the different panels

over. The Hanks and Kanamori (1979) relation was used to compute seismic moment from M_W and the observed seismic moment rate of events with M_W 5.5 and over ($M_0 R_{oss5.5}$) was computed as well (Fig. 4).

As the above $M_0 R_{oss}$ does not represent the total seismic moment rate, the Gutenberg–Richter relation was calculated for the four domains. First, the seismicity rates for each magnitude class were computed by the Albarello and Mucciarelli (2002) approach, where the whole catalogue is divided into time intervals for each of which the probability that it is complete is evaluated and the related rate is weighted accordingly. The Gutenberg–Richter parameters (a and b values) were calculated by the application of the maximum likelihood approach according to the Weichert (1980) procedure. From the Gutenberg–Richter distribution, the individual annual rates were derived and, from them and the M_Ws (from the maximum observed magnitude to 0.1), the calculated seismic moment rate ($M_0 R_{cal}$) was obtained. As this $M_0 R_{cal}$ was calculated considering all the M_Ws, it should represent the actual seismic moment rate released by each domain. In addition, the computed seismic moment rate for events with M_W 5.5 and over ($M_0 R_{cal5.5}$) was also computed. It can be seen from Table 4, where all the results are reported, that the $M_0 R_{cal}$ is larger than the $M_0 R_{oss}$ and the difference varies from one domain to the other from less than two times in the eastern Alps to more than three times in the western Alps. It is notable the situation of the southern Apennines, where $M_0 R_{oss}$ is larger than $M_0 R_{cal}$ because of the large number of moderate-to-large earthquakes which occurred there in the last three centuries. Increasing the time period over which the calculation is done the value of $M_0 R_{oss}$ decreases notably (e.g.: it is 12.0×10^{17} when calculated considering the last five centuries). Moreover, it is quite interesting to observe which is the contribution in terms of $M_0 R_{cal}$ given by the strong earthquakes (M_W 5.5 and over) in each domain. Also in this case the ratio spans over a large interval: strong earthquakes contribute largely in the eastern Alps and in the southern Apennines, where their presence is frequent, while their contribution is limited in the other two domains.

The final comparison refers to the ratio between $M_0 R_{cal}$ and $M_0 R1$ and quantifies the amount of strain which is supposed to be released seismically. This ratio is quite constant around 20–30% with the exception of the western Alps, where it is about 60%. Bressan and Bragato (2009) have found that a significant part of the deformation occur aseismically in the eastern Alps.

In summary, the comparison among the three estimates of $M_0 R$ shows that: (1) $M_0 R_{cal}$ is much larger than $M_0 R_{oss}$, with the exception of the southern Apennines; (2) $M_0 R1$ is larger (about four times) than $M_0 R_{cal}$, with the exception of the western Alps. These values will be introduced in the following computations. More precisely, the part of the $M_0 R$ which is supposed to be released aseismically (obtained from $M_0 R_{cal}/M_0 R1$ in Table 4) will be subtracted from $M_0 R1$ in the analysis that refers to the domains. The ratio between the total moment rate from the finite element model and the seismic moment rate for $M_w \geq 5.5$ is 1.06. So, this correction is applied, subtracting 6% from $M_0 R2$ in the analysis referring to the seismogenic areas. The $M_0 R$ that refers to the distributed seismicity (events with an

Table 4 Annual $M_0 R$s (in N·m/year) and b values (with related standard deviation) for the four domains

Domain	b value	σb	$M_0 R1$ ($\times 10^{17}$)	$M_0 R_{oss}$ ($\times 10^{17}$)	$M_0 R_{oss5.5}$ ($\times 10^{17}$)	$M_0 R_{cal}$ ($\times 10^{17}$)	$M_0 R_{cal5.5}$ ($\times 10^{17}$)	$M_0 R_{cal5.5}$ /M$_0 R_{cal}$	$M_0 R_{cal}$ /M$_0 R1$
E Alps	1.13	0.15	5.6	0.62	0.49	1.17	0.85	0.73	0.21
W Alps	1.50	0.13	6.2	1.07	0.69	3.89	0.70	0.18	0.63
N Apen.	1.44	0.10	19.8	1.93	1.35	5.33	1.63	0.31	0.27
S Apen.	1.09	0.06	76.7	15.7	14.9	14.5	9.37	0.85	0.19

$M_0 R1$ is the geodetic value (see Table 2), $M_0 R_{oss}$ is the value observed in the last three centuries (see Fig. 4) according to the Italian earthquake catalogue (Gruppo di lavoro CPTI 2004), $M_0 R_{oss5.5}$ is the same as $M_0 R_{oss}$ but referring to earthquakes with an M_W 5.5 and over, $M_0 R_{cal}$ is the value calculated from the Gutenberg–Richter relation for all M_Ws, $M_0 R_{cal5.5}$ is the same as $M_0 R_{cal}$ but calculated for earthquakes with an M_W 5.5 and over

$M_W < 5.5$), which is not considered in M_0R2 (Barba, personal communication), can be calculated from the ratio between the M_0R released by large earthquakes and that released by all earthquakes ($M_0R_{cal5.5}/M_0R_{cal}$ in Table 4) and it is added to M_0R2 before the computations. Conversely, M_0R1 does not need any addiction, as it is comprehensive of the earthquakes of all magnitude. As the geophysical model is satisfactorily constrained only for the Apennines, we will restrict the following elaborations only to the seismogenic areas along the Apennines.

5 Definition of faults inside the seismogenic areas

Our knowledge of the seismogenic faults in Italy is far from complete. Hence an ability to account for unmapped faults in seismic hazard models is highly advantageous. Seismogenic areas in Italy are often empty (no mapped faults within) or partially filled with mapped faults. A statistical procedure was developed by Stirling et al. (2007) to fill the empty space of the seismogenic areas with modelled faults with parameters equivalent to those of the mapped faults. The procedure for defining the modelled faults is of Monte Carlo type, and therefore takes account of all the uncertainties in parameters from the mapped faults. In the end, a distribution of modelled fault source parameters is defined, enabling probabilities of specific rupture parameters to be obtained from the distribution.

Entering into detail, each of the four domains contains a certain number of seismogenic areas. Each seismogenic area contains a certain number of mapped faults; the empty space is the difference between the length of the seismogenic area and the sum of the lengths of the mapped faults. This empty space is filled by modelled faults, whose dimensions are simplistically assumed to mimic those [mean and standard deviation (σ)] of the mapped faults present in the domain. The average value of the length of the mapped faults in each domain is, then, considered representative also of the length of the modelled faults in that domain, and the length of these modelled faults is allowed to vary in the range given by the average length of the mapped faults $\pm$ 1 σ. The procedure for filling each empty space of the seismogenic areas is of the Monte Carlo type, in our case with 1,000 repetitions. The algorithm samples the rupture length repeatedly and randomly between the minimum (mean $-$ 1 σ) and maximum (mean $+$ 1 σ) values, and each sample is used to calculate a set of realistic earthquake rupture lengths that fill the empty space of the seismogenic area. The rupture lengths are assumed to be positioned end-on-end, meaning that no overlapping ruptures are assumed. A random number generator producing uniformly distributed random numbers between 0 and 1 [subroutine Random1 in Press et al. (1992)] was the basis for sampling the range, using the extreme endpoints $\pm$ 1-σ values for sampling the average rupture.

In the end, we obtain a set of modelled faults, which mimic the distribution of the mapped faults and fill the empty space of each seismogenic area of each domain.

The number of faults of a specific rupture length in each seismogenic area is given, then, by the sum of the numbers of mapped ($N1_i$) and modelled ($N2_i$) faults, and the total number of faults of a specific rupture length in each domain (N^*_i) is obtained summing up the number of faults in each seismogenic area:

$$N^*_i = \sum_{j=1}^{N_{SA}} \left(N1_{i_j} + N2_{i_j}\right) \tag{2}$$

where N_{SA} is the number of seismogenic areas in the considered domain.

An example of the approach followed for the definition of the modelled faults and the associated parameters is shown for the eastern Alps domain in Table 5 and Fig. 5. This domain contains eight seismogenic areas (purple boxes in Fig. 5a), each of which can or cannot contain mapped faults (red boxes in Fig. 5a); the number of mapped faults in each seismogenic area is reported in Table 5 according to its characteristic magnitude derived by its rupture length (Wells and Coppersmith 1994).

The mean length of the mapped faults is 11.96 km with a σ of 4.65 km. After the Monte Carlo simulations, the resulting number of modelled faults is reported in Table 5. Figure 5b shows the combined result for the modelled and mapped

Table 5 Number of mapped and modelled faults in the eastern Alps domain

M_W	SA_007		SA_060		SA_061		SA_062		SA_064		SA_065		SA_066		SA_067		Total	
	Mod.	M.	Mod.	M.	Mod.	M.	Mod.	M.	Mod.	M.	Mod.	M.	Mod.	M.	Mod.	M.	Mod.	M.
5.5	0.000	1	0.000	0	0.000	0	0.000	0	0.000	0	0.000	0	0.000	0	0.000	0	0.000	1
5.6	0.000	0	0.000	0	0.000	0	0.000	0	0.000	0	0.000	0	0.000	0	0.000	0	0.000	0
5.7	0.000	0	0.000	0	0.000	0	0.000	0	0.000	0	0.000	0	0.000	1	0.000	0	0.000	1
5.8	0.000	0	0.000	0	0.000	0	0.000	0	0.000	1	0.069	0	0.000	0	0.181	0	0.250	1
5.9	0.000	0	0.000	0	0.000	0	0.000	1	0.306	0	0.267	0	0.000	0	0.263	0	0.836	1
6.0	0.256	0	0.015	0	0.127	0	0.000	0	0.826	0	0.250	0	0.000	1	0.270	0	1.744	1
6.1	0.606	0	0.182	1	0.238	1	0.000	0	0.977	0	0.332	0	0.000	0	0.299	0	2.634	2
6.2	0.138	0	0.302	0	0.283	0	0.000	0	1.047	0	0.083	0	0.000	0	0.122	0	1.975	0
6.3	0.000	0	0.319	0	0.326	0	0.000	0	0.355	0	0.000	0	0.000	0	0.000	0	1.000	0
6.4	0.000	0	0.260	1	0.054	0	0.000	0	0.000	0	0.000	1	0.000	0	0.000	0	0.314	2
6.5	0.000	0	0.062	1	0.000	0	0.000	1	0.000	0	0.000	0	0.000	1	0.000	0	0.062	3
6.6	0.000	2	0.000	0	0.000	0	0.000	0	0.000	0	0.000	0	0.000	0	0.000	0	0.000	2

The number of seismogenic areas refers to Fig. 5a.

Mod. indicates the modelled faults (i.e.: resulting number from the Monte Carlo simulations divided by 1000), *M*. the mapped ones

fault sources. The distribution of the modelled faults shows a Gaussian pattern with central tendency around magnitude 6.1. The number of modelled faults is larger than that of the mapped faults around magnitude 6.1 while it is minimal at the edges of the distribution. Some peculiar features are given by the number of mapped faults: no faults referring to magnitude 6.2 and 6.3 have been identified yet in this domain while the number of those of exceeding magnitude 6.4 and larger is notable.

6 Geodetic constraints on seismicity rates

Our approach is to convert $M_0 R$ for each domain into earthquake magnitude and frequency. The earthquakes are assumed to be described by the

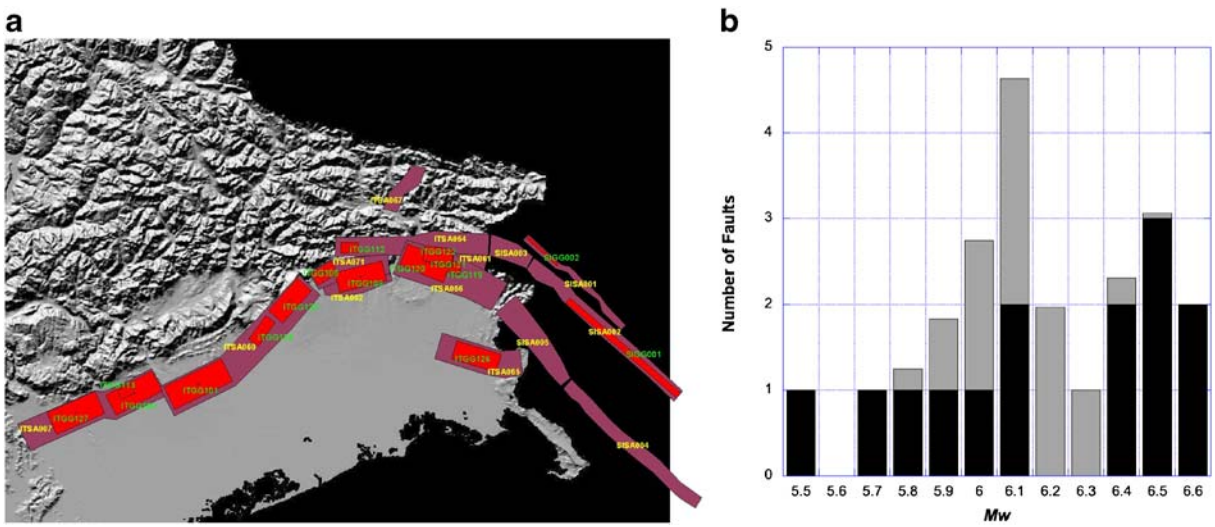

Fig. 5 Mapped and modelled faults in the eastern Alps domain: **a** seismogenic areas (*purple areas* marked by ITSA) and mapped faults (*red areas* marked by ITGG), **b** magnitude distribution (*black columns* for the mapped faults and *grey columns* for the modelled faults)

characteristic earthquake model on a given fault, and these characteristic earthquakes collectively describe a Gutenberg–Richter distribution at a regional scale (i.e. within each domain, or Italy as a whole). We also calculate distributed earthquake recurrence parameters for each domain from a combination of catalogue seismicity and geodetic observations. Gutenberg–Richter b values of each domain are computed from the seismicity observed in the domain itself, while the a value of each domain can be obtained from the geodetic observations, i.e. from the M_0R in the domain. In fact,

$$\log N' = a' - b' \log M_0 \tag{3}$$

where N' is the number of earthquakes with seismic moment larger than, or equal to, M_0, where

$$a' = a + \frac{9.1}{1.5} b \tag{4}$$

and

$$b' = \frac{1}{1.5} b \tag{5}$$

considering the relation between magnitude, M_W, and M_0 in N·m (Hanks and Kanamori 1979):

$$\log M_0 = 9.1 + 1.5 M_W \tag{6}$$

Knowing the value of the M_0R in the domain under study, in our case obtained from the geodetic observations, and fixing the maximum value for M_0, derived from the maximum magnitude for that domain, we can write:

$$M_0 R = \sum_i N_i M_{0_i} \tag{7}$$

where N_i is the unknown annual non-cumulative number of earthquakes with M_{0i}, and the index i represents all the classes of M_0 in the domain.

From Eq. 3 we have

$$N'_i = 10^{a' - b' \log M_{0_i}} \tag{8}$$

where N'_i is the cumulative number of earthquakes with M_{0i} and above.

From the cumulative number we can compute the non-cumulative number N_i:

$$\begin{aligned} N_i = N'_i - N'_{i+1} &= 10^{a' - b' \log M_{0_i}} - 10^{a' - b' \log M_{0_{i+1}}} \\ &= 10^{a'} \left(\frac{1}{10^{b' \log M_{0_i}}} - \frac{1}{10^{b' \log M_{0_{i+1}}}} \right) \end{aligned} \tag{9}$$

Substituting the value of N_i given by Eq. 9 into Eq. 7, we obtain an equation where the only unknown term is the a' value. In such a way we can compute the a' value in the domain under study from strain instead of from seismicity and, consequently, we can obtain the a value from Eq. 4, and the number of earthquakes, N_i, for all classes of seismic M_{0i} from Eq. 9.

In agreement with the identification of faults (mapped and modelled) inside the seismogenic areas introduced in the previous section and considering the existing equivalence between M_0 and fault rupture length, obtained by the application of the Wells and Coppersmith (1994) and Hanks and Kanamori (1979) scaling laws, in each domain, the number of earthquakes, N_i, of a specific class of M_{0i} is given by the product of the number of faults of a given rupture length [N^*_i in Eq. 2] and the related rate of occurrence, ν_i

$$N_i = N^*_i \cdot \nu_i \tag{10}$$

In such a way, we can compute the rate of occurrence for each class of M_0. This rate will determine a regional Gutenberg–Richter distribution (i.e.: in the domain), while the Gutenberg–Richter distribution will not be reflected inside the seismogenic areas.

In summary, our procedure defines a suite of mapped and modelled fault sources inside each seismogenic area, each with a defined fault source length and, consequently, with a characteristic M_0. From the M_0R obtained from geodetic observations, we constrain the occurrence rate for each class of M_0. The earthquake recurrence for fault sources within seismogenic areas is defined according to the characteristic earthquake model, and the distributed seismicity parameters for the surrounding domains are modelled according to the Gutenberg–Richter relationship.

7 Geophysical constraints on seismicity rates

We also use strain rates produced through numerical modelling by Barba (2007). Such strain rates are those corresponding to the least misfit between geodetic (Caporali 2007; Serpelloni et al. 2007) and stress data (Montone et al. 2004) and the numerical predictions produced by trial-and-error, using thin-shell finite element code SHELLS (Bird 1999), in a large number of iterations which mostly differ by boundary conditions, fault friction coefficient [as for example in Barba et al. (2008, 2009)].

The technique gives a value of the M_0R for each seismogenic area and, consequently, the computation refers to each seismogenic area instead of to each domain. In the geodetic constraint approach the characteristic earthquakes of the mapped and modelled faults form a Gutenberg–Richter distribution in the domains but not necessarily inside the seismogenic areas. Differently, in the geophysical constraint approach, the characteristic earthquakes of the mapped and modelled fault sources defined inside each seismogenic area collectively produce a Gutenberg–Richter distribution. The observation of a Gutenberg–Richter distribution for large regions, countries, and the globe is well documented (e.g. WGCEP 1995; Stirling et al. 1998).

8 Application

As a working hypothesis it is assumed that only earthquakes with M_W 5.5 and above occur in the seismogenic areas, and while the M_0R calculated from geodetic observations represents the regional total value (i.e.: earthquakes in the seismogenic areas plus distributed seismicity plus aseismic creep), the M_0R obtained from the geophysical modelling refers to the seismicity of the seismogenic areas only. In the geodetic constraint case, the percentage of M_0R accommodated as an aseismic creep was taken from Table 4 (column 10), while the distributed seismicity is represented by the Gutenberg–Richter relation for events of M_W less than 5.5. [Eq. 7 applies to the whole range of M_0 (i.e., M_W in the range 0–M_{max}) although only events related to M_W 5.5 and larger are treated in the computation of probabilities]. In the geophysical modelling case, the percentage of moment rate related to the distributed seismicity is derived from Table 4 (column 9) and added to the value calculated from the modelling (that refers only to events with an M_W 5.5 and larger). In both cases a regional b value is assumed for the earthquake rate calculations (see Table 4). The Poisson distribution is then used to estimate the probability of exceeding magnitude m in t years, $F_{Mt}(m)$:

$$F_{M_t}(m) = P[M_t > m] = 1 - e^{-\nu t} \tag{11}$$

where ν is the annual rate of magnitude m and over. This approach is applied to four domains covering Italy and for which the regional M_0R can be computed. The number of events for each M_0 class was determined according to Eq. 10 and it was then scaled in the seismogenic areas according to Eq. 2. The cumulative rate for each magnitude class is obtained in such a way, and the associated probabilities were computed for exceeding different magnitude classes inside each seismogenic area.

The approach based on the geophysical constraints was applied directly considering the seismogenic areas.

9 Results

We show our 30-year probability for $M_W \geq 6.0$ and ≥ 6.5 in Table 6 and Figs. 6 and 7, obtained by way of the geodetic constraints and derived from the geophysical modelling. It is interesting to note that there is no direct proportionality between the forecasts for M_W 6.0 (Fig. 6) and 6.5 (Fig. 7): this is due to the fact that the seismogenic areas are supposed to be composed of faults which behave according to the characteristic earthquake model. Consequently, the probability distribution of each seismogenic area is strongly peaked at specific magnitude values, e.g.: the characteristic magnitudes of the faults existing there. A clear example is given by the probabilities of the two seismogenic

Table 6 Exceedance probability in 30 years for magnitude 6.0 and 6.5

SA ID	Lon. E	Lat. N	P1–6.0	P1–6.5	P2–6.0	P2–6.5
CHSA001	7.974	46.301	0.014			
CHSA002	7.255	46.117	0.013			
FRSA001	6.655	44.706	0.013			
ITSA001	11.826	44.231	0.010	0.001		
ITSA002	9.820	45.438	0.014	0.003	0.011	0.001
ITSA003	15.161	41.699	0.080	0.031	0.003	0.001
ITSA004	15.965	41.287	0.177	0.002	0.007	
ITSA005	16.333	40.642	0.051		0.013	
ITSA007	11.690	45.766	0.031	0.014		
ITSA008	13.578	43.541	0.007		0.009	
ITSA009	10.270	44.824	0.014	0.001		
ITSA010	12.035	44.743			0.015	0.002
ITSA011	12.045	44.348	0.011			
ITSA012	12.080	44.567	0.014	0.001	0.015	0.002
ITSA013	13.975	41.870	0.035		0.023	
ITSA014	13.180	38.339	0.039	0.036	0.085	0.027
ITSA015	16.249	39.375	0.113		0.097	
ITSA016	15.599	38.103	0.030	0.030	0.007	0.007
ITSA018	9.146	44.997	0.014	0.001		
ITSA019	17.016	39.294	0.035	0.025	0.035	0.006
ITSA020	13.664	42.990	0.010		0.084	
ITSA022	7.767	43.880	0.022	0.001		
ITSA023	7.385	44.890	0.011			
ITSA024	14.605	41.382	0.085	0.054	0.130	0.017
ITSA025	13.382	42.263	0.044	0.035	0.100	0.014
ITSA026	10.150	44.299	0.040			
ITSA027	12.374	43.684	0.080	0.026	0.085	0.011
ITSA028	12.835	43.069	0.024		0.022	
ITSA030	12.696	44.073				
ITSA031	13.698	43.580	0.010		0.015	
ITSA032	13.053	43.754	0.021		0.030	
ITSA033	16.237	39.789	0.048		0.016	
ITSA034	15.540	40.575	0.215	0.092	0.210	0.020
ITSA037	12.277	43.384	0.021		0.008	0.001
ITSA038	15.954	40.040	0.086		0.099	0.004
ITSA039	12.494	44.047	0.009			
ITSA040	13.427	42.460	0.039		0.103	
ITSA041	12.178	43.547				
ITSA042	14.990	38.309	0.094	0.029	0.033	0.004
ITSA043	13.145	43.877	0.009		0.018	
ITSA044	9.643	45.124	0.014			
ITSA045	9.919	44.815	0.014	0.005		
ITSA046	10.520	44.561	0.014	0.001		
ITSA047	11.424	44.425	0.014	0.001		
ITSA048	10.777	45.771	0.022			
ITSA049	10.727	44.810	0.015			
ITSA050	11.508	44.869	0.014	0.001		
ITSA051	11.212	44.794	0.014	0.001	0.010	0.001
ITSA052	14.780	42.946	0.010			
ITSA053	16.099	38.479	0.131	0.044	0.116	0.022
ITSA054	13.898	43.016	0.008		0.012	
ITSA055	15.918	38.228	0.140		0.027	
ITSA056	12.493	43.279	0.041		0.026	

Table 6 (continued)

SA ID	Lon. E	Lat. N	P1–6.0	P1–6.5	P2–6.0	P2–6.5
ITSA057	15.040	41.243	0.064	0.064	0.001	0.001
ITSA058	15.837	41.717	0.149		0.003	
ITSA059	14.750	42.179	0.137		0.010	
ITSA060	12.330	45.982	0.046	0.005		
ITSA061	13.240	46.262	0.036			
ITSA062	12.836	46.205	0.004	0.004		
ITSA063	15.494	40.873	0.037	0.015	0.073	0.010
ITSA064	13.082	46.306	0.021			
ITSA065	13.391	45.969	0.023			
ITSA066	13.255	46.215	0.032	0.004		
ITSA067	13.042	46.477	0.013			
ITSA068	16.357	38.817	0.047	0.007	0.044	0.003
ITSA070	16.579	41.635	0.036	0.028		
ITSA071	12.806	46.218	0.004	0.004		
ITSA075	13.925	42.492	0.009		0.010	
ITSA077	14.510	41.660	0.030	0.030	0.001	0.001
ITSA079	14.613	41.989	0.042	0.012	0.022	0.002
ITSA080	16.164	38.434	0.141		0.012	
ITSA084	15.302	41.041	0.052	0.052	0.003	0.003
ITSA087	15.356	40.855	0.048		0.044	
ITSA089	15.881	40.969	0.095	0.002	0.004	
SISA001	13.838	46.201	0.008			
SISA002	13.945	46.055	0.024	0.014		
SISA003	13.525	46.291	0.003			
SISA004	14.074	45.705	0.008			
SISA005	13.628	46.019	0.009			

P1 indicates the results obtained with geodetic constraints, P2 those with geophysical constraints. The name of the seismogenic areas (SA ID) is made up of the country code (CH for Switzerland, FR for France, IT for Italy, SI for Slovenia) followed by SA, and the code number of the seismogenic area

areas along the northern coast of Sicily according to the geodetic constraint: the eastern one shows a higher probability for $M_W \geq 6.0$ (Fig. 6a), while the western one does for $M_W \geq 6.5$ (Fig. 7a). This aspect simply shows that events with an $M_W \geq 6.5$ are more likely to occur along the western sector, while events with an M_W between 6 and 6.5 are largely more probable along the eastern one.

The 30-year probability for $M_W \geq 6.0$ based on our geodetic modelling approach (Fig. 6a) is low everywhere and varies in one seismogenic area to another mainly from 1% to 5%. Most of the most 'hazardous' seismogenic areas (in terms of earthquake probabilities) are located in the southern Apennines (black large dots in Fig. 6a, corresponding to a probability greater than 5%). The equivalent probabilities in the case of the results obtained from the geophysical modelling approach (Fig. 6b) are very similar to those with geodetic constraints (Fig. 6a) showing almost the same seismogenic areas. Some disagreements can be noted along the Adriatic coast, where the forecasts from the geophysical modelling are higher than those from the geodetic model in the central sector and lower in the southern one. In the southern sector, the geophysical model has been mainly constrained through Serpelloni et al. (2007) geodetic data, showing a moment rate that is lower than the moment rate relative to the geodetic data used to derive the earthquake rates within this work. We consider the probabilities derived by the current geodetic data more reliable than those derived by the geophysical model in the southeastern side of the peninsula as the current data are greater in number and more accurate. The largest probabilities for $M_W \geq 6.0$ are found in the southern Apennines, where they reach values between 10% and 20% (Fig. 6b).

The 30-year probability for $M_W \geq 6.5$ (Fig. 7) is obviously very low again and varies mainly between 0.4% and 3%. The agreement between the estimates according the two approaches is again fairly good, although the estimates under

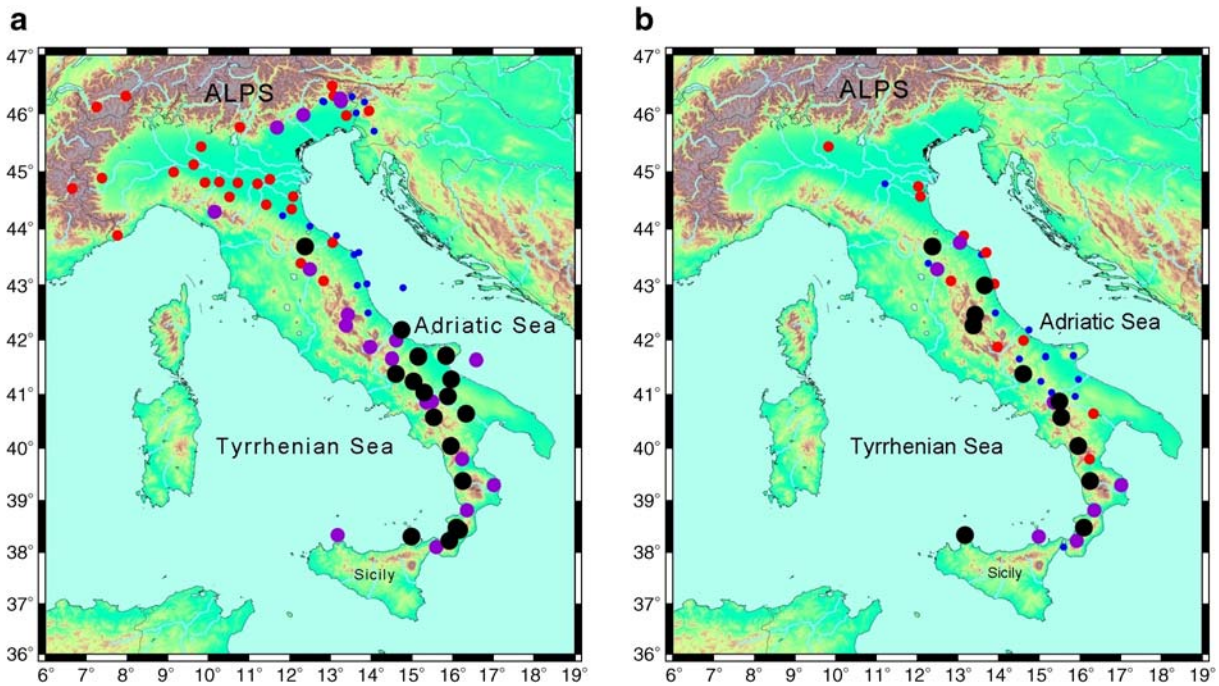

Fig. 6 Thirty-year probability for $M_W \geq 6.0$ according to a Poisson model: **a** computed by geodetic constraints, **b** computed by geophysical constraints. *Blue small dots* for $P \leq 1\%$; *red medium dots* $1\% < P \leq 2.5\%$; *purple medium circles* $2.5\% < P \leq 5\%$, *black large circles* $P > 5\%$

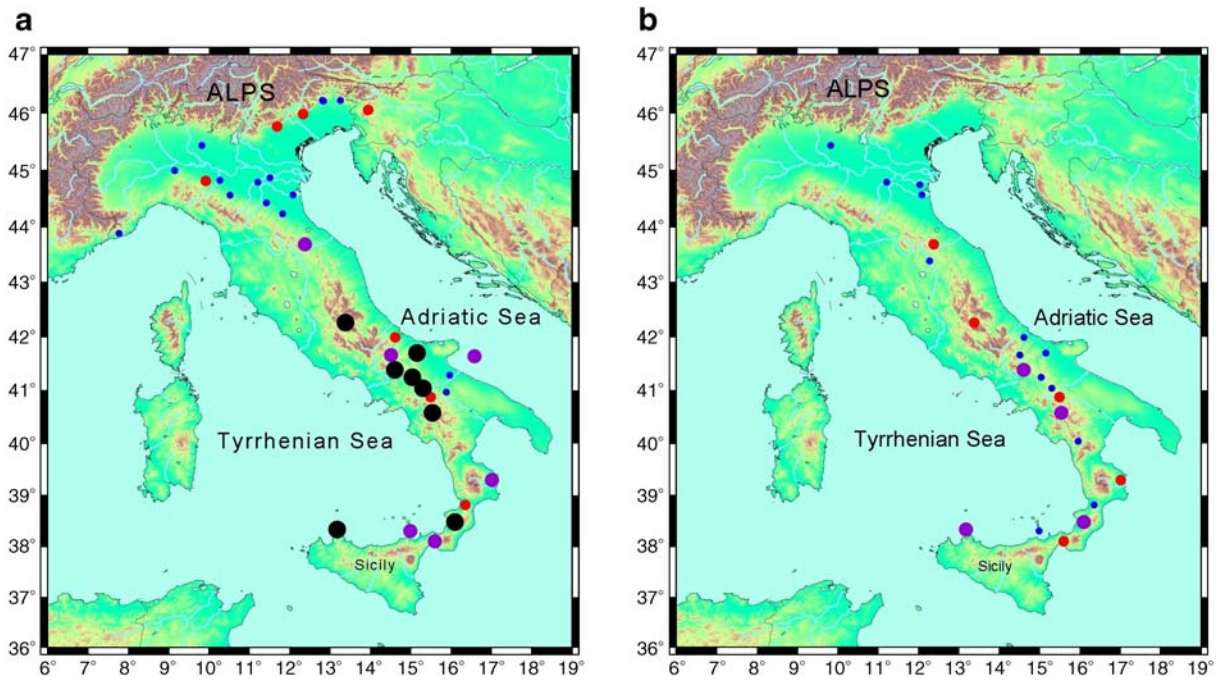

Fig. 7 Thirty-year probability for $M_W \geq 6.5$ according to a Poisson model: **a** computed by geodetic constraints, **b** computed by geophysical constraints. *Blue small dots* for $P \leq 0.4\%$; *red medium dots* $0.4\% < P \leq 1.5\%$; *purple medium circles* $1.5\% < P \leq 3\%$, *black large circles* $P > 3\%$

geophysical constraints are slightly lower. Again a disagreement can be noted in a small sector of the southern Apennines. The largest probabilities are found again in the southern Apennines, where they reach values lower than 10%.

Figure 8 shows the differences between the estimates obtained by considering the two different constraints and quantifies how much the results with the geodetic constraints differ from those from geophysical modelling. Considering $M_W \geq$

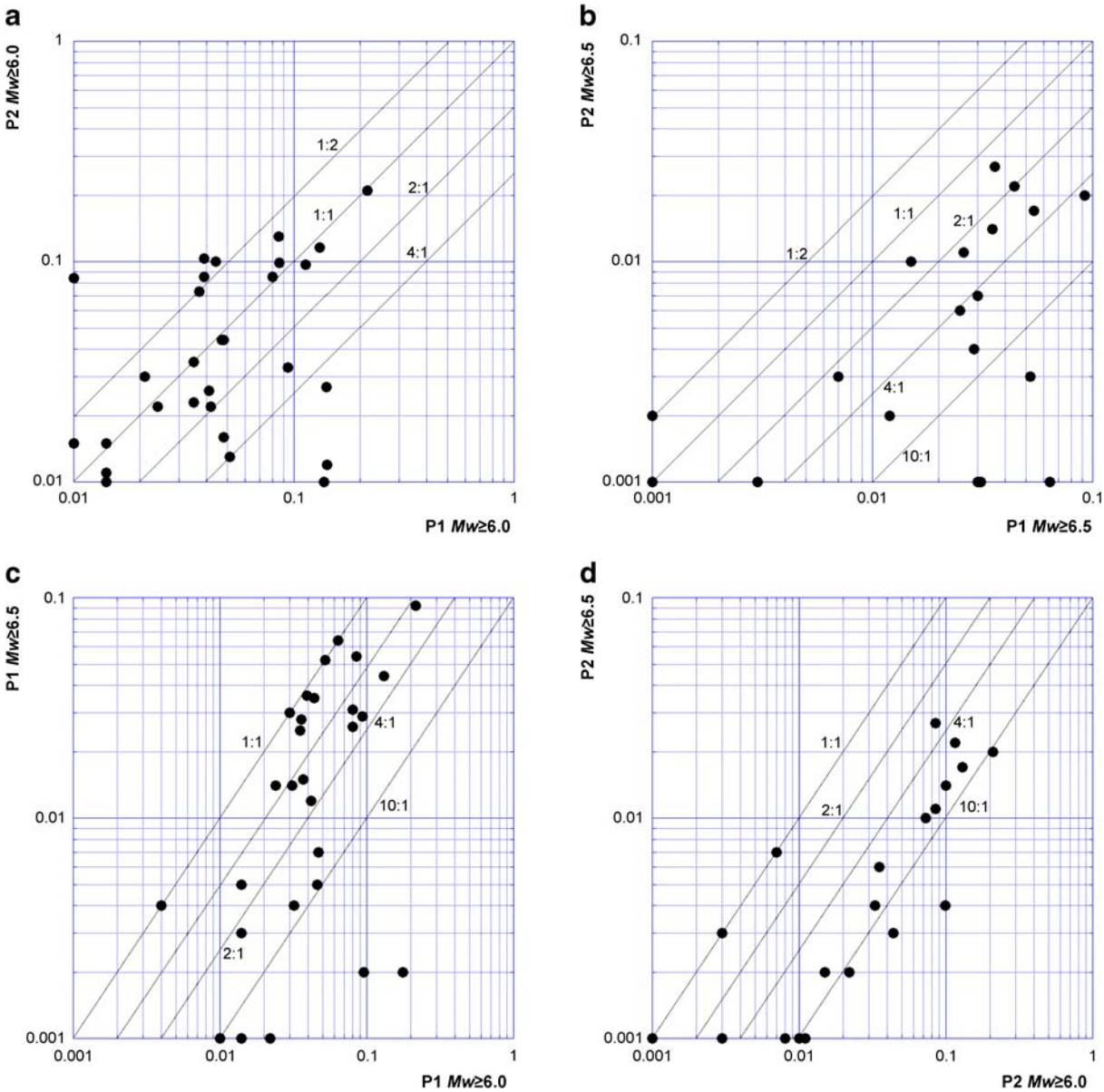

Fig. 8 Comparison of the probability estimates ($P1$ indicates the exceedance probability in 30 years computed with geodetic constraints, $P2$ indicates the exceedance probability in 30 years computed with geophysical constraints): **a** P2 vs. P1 for M_W 6.0, **b** P2 vs. P1 for M_W 6.5, **c** P1 for M_W 6.5 vs. P1 for M_W 6.0, **d** P2 for M_W 6.5 vs. P2 for M_W 6.0

6.0 (Fig. 8a), it can be seen that the great majority of points remain within the lines indicating the ratios 1:2 and 2:1, that is where the results with one approach are less than double those with the other approach. There are a few among the remaining points where the estimates with geodetic constraints are by far larger (more than four times) than those taken from geophysical modelling. The situation is worse when events with an $M_W \geq 6.5$ are considered (Fig. 8b). In this case, almost all forecasts with geodetic constraints are larger than those from geophysical modelling and even values 10 times and larger are obtained in a few cases.

The only region where the estimates with the two approaches, referring to $M_W \geq 6.0$ and $M_W \geq 6.5$ as well, differ greatly is the promontory in the southern Adriatic sea (Gargano promontory). There, the forecasts from the geophysical modelling are much lower than those with geodetic constraints: this difference is notably larger than that in the rest of Italy.

Some explanations for the differences shown by the two approaches can be suggested. Both methods suffer some limitations: the geodetic one because it was possible to compute the strain rate over wide regions (the four domains, see Appendix A) and some peculiar differences are, consequently, lost. The geophysical modelling is not yet perfectly tuned and a satisfactory agreement with all the boundary conditions is not reached yet (see Appendix B).

The lack of proportionality between the estimates referring to a different magnitude threshold has been already justified, and is more evident in the case of a geodetic constraint (Fig. 8c) than when data from the geophysical modelling have been used (Fig. 8d). The latter, in fact, display quite a nice alignment along the line 10:1, indicating that the probability of $M_W \geq 6.0$ is about 10 times larger than that of $M_W \geq 6.5$.

10 Conclusions

We have developed two new approaches to estimating earthquake probabilities for moderate-to-large earthquakes in Italy, using geodetic and geophysical modelling methods. The two approaches show a good agreement in the resulting probabilities, with noticeable differences only in limited areas of Italy. Thirty-year probabilities both based on geodetic and geophysical constraints are less than 5% for $M_W \geq 6.0$ with the exception of the southern Apennines, where they reach values between 10% and 20% in a very few seismogenic areas. In the same areas, 30-year probabilities for $M_W \geq 6.5$ remain lower than 10%. Future work will be focused on improving the methodologies developed, in an effort to constrain better the derived earthquake probabilities.

Acknowledgements The present study has been developed in the framework of the projects of interest for the Italian Department of Civil Protection and financed by the National Institute of Geophysics and Volcanology. Many thanks are due to Roberto Basili, INGV Rome, who helped us with his great expertise in the data treatment of the Database of the Italian Seismogenic Sources, and Laura Peruzza, OGS Trieste, and Steven Ward, University of California at Santa Cruz, for valuable discussions. We wish to express our deep gratitude to David Perkins, USGS Denver, and to an anonymous reviewer, both have greatly improved this paper with their valuable suggestions and remarks. Most of the figures were produced using the Generic Mapping Tool (GMT) software package (Wessel and Smith 1991).

Appendix A: Geodesy

A1 Validation of GPS velocity data

The analysis of GPS data normally rests on the IGS standards: these prescribe consistent orbits and Earth Rotation Parameters, and recommend models for Phase Center Variations of the antennas, the elevation cutoff angle and a set of datum defining coordinates and velocities. The final product of the adjustment must be available in the SINEX format and the constraints adopted in the adjustment must be explicitly given, so that further analyses can be made with possibly different constraints.

An example of this procedure is given by the weekly maintenance of the European Reference Frame done by the European Permanent Network (http://www.epncb.oma.be): 16 local analysis centers (LACs) process partially overlapping sub-networks of several tens of permanent GPS stations in Europe. The 16 weekly solutions in

SINEX format and with removable constraints are combined into one network solution by an independent combination center. The constraints imposed by the individual analysis centers are removed and new constraints are imposed, so that the final adjustment is properly aligned with the IGS reference frame. The comparison of the individual sub-network solutions with the final network solutions yields a quantitative estimate of the mutual consistency of the processing strategies of the LACs. Typical discrepancies between solutions are at the sub millimeter level in translation, fraction of milliarcsec in rotation and few parts per billion in scale. Furthermore, local analysis centers process regional networks, e.g. at a national level, of permanent GPS stations using the same standards as for the EPN sub-networks. This results in additional SINEX files, which may be combined with the EPN SINEX files at corresponding epochs for network densification. Several software packages are available for such combination work: Bernese's ADDNEQ or ADDNEQ2, CATREF, GIPSY, GLOBK are well-known examples. The SINEX format has the advantage that is a software independent format. Hence SINEX files, if generated by a standardized processing, can be considered a form of metadata of higher level than the RINEX files containing raw phase and pseudorange data.

The rest of this appendix analyses velocities and derived products (velocity field, strain rate) of permanent GPS stations resulting from a combination of the weekly SINEX files concerning the EPN, an Italian network processed by the University of Padua (UPA) and an Austrian network processed by the Astronomical Observatory in Graz (GP_). Both Padova and Graz are EPN Local Analysis Centers.

The SINEX used in the combination analysis are summarized as follows:

- European network (EUR<GPSwk>.SNX) from GPS week 860 to 1380 (~1996 to 2006);
- Italian Network (UPA<GPSwk>.SNX) from GPS week 995 to 1380 (~1999 to 2006);
- Austrian Network (GP_<GPSwk>.SNX) from GPS week 995 to 1380 (~1999 to 2006).

Beginning GPS week 995, the three normal equations are combined with the program ADDNEQ of the Bernese Software v.4.2 and the appropriate constraints are imposed on those stations with position and velocities listed in the ITRF2000 solution. Because our combination scheme fully considers the variance covariance matrix of the individual network solutions, also the non-ITRF2000 stations have coordinates consistently defined with that system. To ensure that the EPN solution is the backbone, the weight of its SINEX files is larger than for the UPA and GP_ solutions

A total of 372 permanent GPS stations are present in the combined network, although only for a fraction of them a reliable estimate of the velocity can be made. The ITRF2000 (Altamimi et al. 2002) constraints in position and velocity of the datum defining stations are available at http://itrf.ensg.ign.fr/ITRF_solutions/2000/sol.php. The datum defining stations are listed below, and are chosen on the basis of their continuous tracking for several years. Figure 9 shows the velocities of stations with sufficiently reliable time series (2.5 years minimum), which were used in the subsequent strain rate analysis.

A2 Statistical properties of the estimated velocities

The horizontal velocities estimated in the ITRF2000 frame exhibit a dominant NE trend of the order of 2 cm/year. Most of this signal can be accounted for with a rigid rotation about an Eulerian pole and can be filtered out. The residual velocities (Fig. 9) are spatially correlated: the likelihood that two stations have similar velocities decreases with increasing distance between the two stations. This likelihood function is shown in Fig. 10 and forms the basis for computing a velocity field and strain rates out of the observed velocities. According to the analytical model shown in Fig. 10, the characteristic distance d_0 is such that the likelihood of velocities of sites at such distance is reduced to 50% that at zero lag. More details are given in Caporali et al. (2003).

Once the velocities and their uncertainties are given at each GPS station, and the correlation function has been specified, the velocities and their uncertainties can be interpolated at other

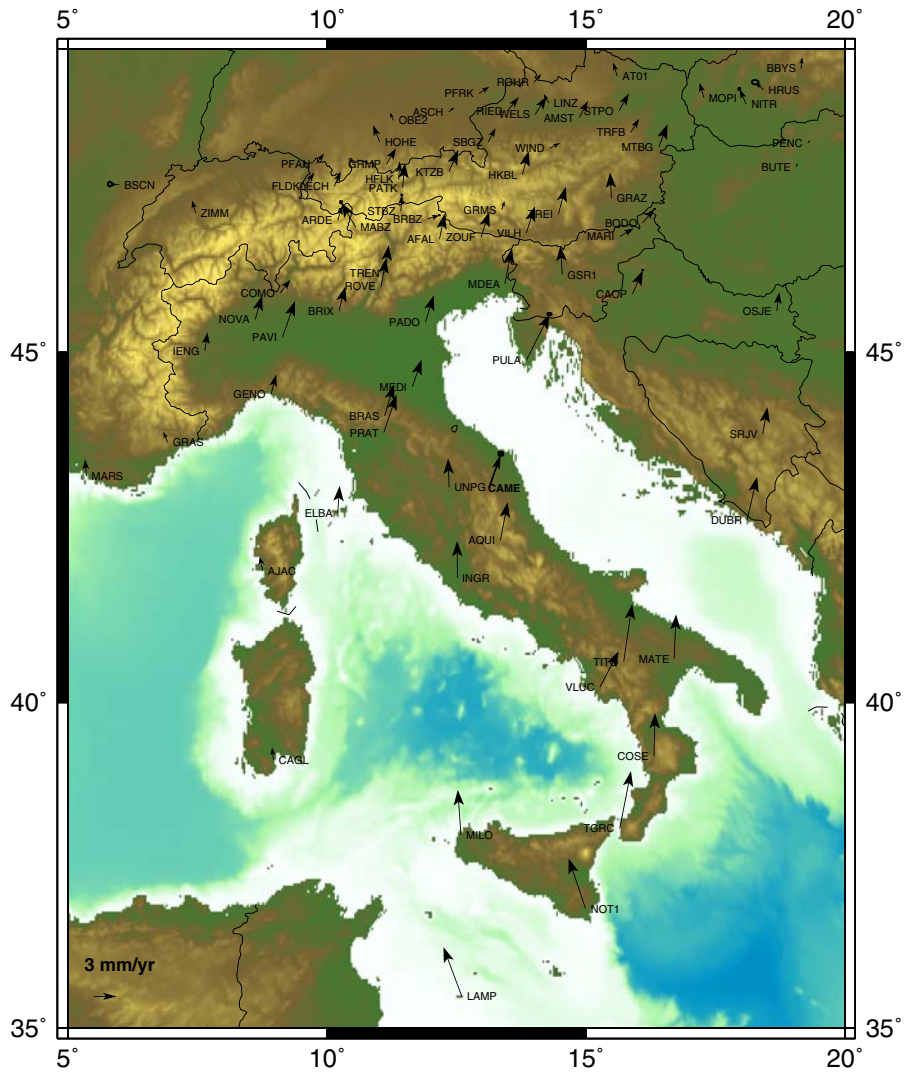

Fig. 9 Horizontal velocities of GPS permanent stations in the Alpine Mediterranean area, after removing a common rigid rotation which approximates the rigid rotation of the Eurasian plate in the ITRF2000 frame. Error ellipses are 2σ. Velocities have been computed only for stations with at least 2.5 years of continuous tracking. Not shown are the velocities of EPN stations falling outside the plotting box

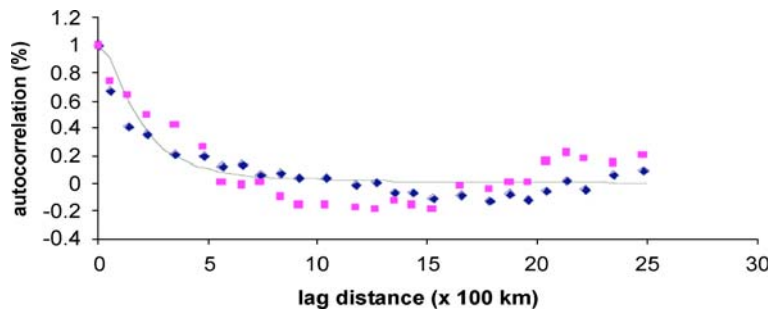

Fig. 10 The autocorrelation of the observed velocities as a function of the distance between stations. The *continuous curve* represents an analytical covariance function depending on the inverse squared distance. The fit to the observed autocorrelation defines a scale distance in the range 150 to 250 km. The cross-correlation is negligibly small

points P by a minimum variance (or 'optimal') algorithm known as least squares collocation:

$$\begin{bmatrix} v_n \\ v_e \end{bmatrix}_P = \sum_s C\left(d_{P,s}\right) \sum_{s'} \left[C\left(d_{s,s'}\right) + W_{ss'}\right]^{-1} \cdot \begin{bmatrix} v_n \\ v_e \end{bmatrix}_{s'}$$
$$s, s' = \text{station} \quad \text{indices} \tag{12}$$

with

$$W_{ss'} = \frac{\frac{1}{\sigma_s^2}}{\sum_{s''} \frac{1}{\sigma_{s''}^2}} \delta_{ss'} \tag{13}$$

The mean velocity is removed prior to interpolation and added back to the interpolated value.

Likewise, the velocity derivatives [Eq. 14] yield a velocity gradient, or strain rate tensor:

$$\begin{bmatrix} v_{n,n} & v_{n,e} \\ v_{e,n} & v_{e,e} \end{bmatrix}_P = \sum_s \begin{bmatrix} \frac{\partial C}{\partial n} & \frac{\partial C}{\partial e} \\ \frac{\partial C}{\partial n} & \frac{\partial C}{\partial e} \end{bmatrix}_{P,s} \times \sum_{s'} \left[C\left(d_{s,s'}\right) + W_{ss'}\right]^{-1} \cdot \begin{bmatrix} v_n \\ v_e \end{bmatrix}_{s'}$$
$$s, s' = \text{station} \quad \text{indices} \tag{14}$$

The fact that the individual velocities have different uncertainties is embodied into the algorithm by augmenting the correlation matrix C between the sites with a weight matrix W built with the variances of the individual velocities. This set up ensures that the resulting velocity field will be smooth. The velocity field, when computed at the location of a GPS station, will be closer to the observed velocities, the smaller the associated uncertainty. In general the weight matrix W acts as a smoother or low pass filter. This ensures that local velocity anomalies, e.g. induced by monument instabilities, will not affect the velocity field or the strain rate.

The components of the strain rate matrix [Eq. 14] are expressed in a geographical frame. The eigenvectors and their azimuth can be computed by standard matrix diagonalization. We consider as extensional the eigenvector with positive eigenvalue.

The estimate of the strain rate involves a differentiation and must be done with great care. While the interpolation of the velocity reduces the noise by smoothing (integration), differentiation tends to amplify the noise, especially over short distances. If two stations separated by a distance d have each an uncorrelated uncertainty s in the velocity, then a quick estimate of the uncertainty in the resulting strain rate is $2^{1/2}\ s/d$. If $s = 0.5$ mm/year and $d = 100$ km, the expected uncertainty is 7 nstrain/year (1 nstrain $= 10^{-9}$). Shorter distances will proportionally increase the uncertainty to levels above the sought for signal, which is of the order of several tens up to 100 of nstrain/year, typically.

It is crucial to identify the optimal locations, from the point of view of minimal variance, where the strain rate can be reliably computed. A first criterion for optimal choice is that there exist uniformly distributed stations in the neighborhood of the computation point. A second criterion is that the nearest stations should be given higher weight than more distant stations, if their velocities have the same variance. This last criterion is automatically satisfied by the collocation algorithm. To ensure that the strain rate is computed at points such that it is sufficiently well constrained by data from neighboring stations we have adopted the following rule: the strain rate is computed at the geographical location of those permanent stations of known velocity, such that at least one additional station with known velocity exists in each quadrant within a radius equal to the correlation distance d_0.

The adopted rule is exemplified in Fig. 11. We require that within a circle of radius d_0 five velocities are defined: the velocity at the center of the circle and at four additional sites. The least squares collocation represents in a continuous form a finite difference between the center velocity and the peripheral velocities. In this manner we ensure that the resulting strain rate reliably describes the rate of deformation in the circled area. Unfortunately the strain rate computed by this rather conservative approach not always relates to areas of seismological interest. Mapping the strain rate to other locations is mathematically feasible but not recommended, due to the fast increase of the variance.

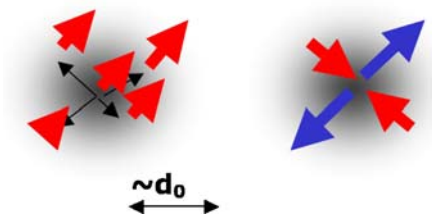

Fig. 11 Example of strain rate calculation. On the *left* figure five sites are present: one is at the center of a circle of radius equal to the typical correlation length of the ensemble of velocities, and four additional velocities are uniformly distributed about that point within the circle. On the *right* we have the corresponding strain rate eigenvectors. The structure of the velocity distribution is such that one expects an extension in the NE–SW direction. This deformation regime is then a mean property of the entire circular area

A3 Numerical results

The numerical results for northern, central, and southern Italy obtained with the velocities of permanent GPS stations resulting from the combined analysis described above were used as geodetic constraints in the computation of the earthquake occurrence probabilities (Table 2). For southern Italy we have a number of stations insufficient to meet the adopted criterion for strain rate computation. Therefore we have used a set of velocities coming from campaign and permanent stations, available from the literature and processed by analysis centers outside the EUREF network. For this reason we have thought it appropriate not mixing the sets of velocities, although the methodologies of computation are, in a broad sense, consistent with each other.

Appendix B: Finite-element modelling

The finite-element modelling aimed to reproduce a large amount of neotectonic data for Italy by means of trial-and-error approach, using thin-shell finite element code SHELLS (Bird 1999), in a large number of iterations which mostly differ by boundary conditions, fault friction coefficient [as for example in Barba (2007) and Barba et al. (2008, 2009)]. In all these studies, model predictions were compared to three independent data sets: geodetic horizontal velocities from temporary and permanent GPS stations (Serpelloni et al. 2007; Caporali 2007); stress regime data, based on relative stress magnitudes, and the directions of maximum horizontal compressive stress (Montone et al. 2004). Residuals between model predictions and the calibration data sets allowed to characterize of the degree of realism of the numerical results. The model results that exhibited the lowest misfits were averaged, thereby accounting for uncertainties in boundary conditions and model parameters. Misfits were standardized to account for the different calibration datasets.

The model incorporates faults and realistic rheology in a two-layer grid (crust and lithospheric mantle) with laterally varying seismogenic thickness, heat flow, and topography. The horizontal components of the momentum equation (Kong and Bird 1995) were solved to predict long-term horizontal velocities, anelastic strain rates, vertically integrated stresses, and fault slip rates.

In the thin-shell neotectonic modelling program SHELLS [Bird (1999) and references therein] uses isostasy and vertical integration of lithospheric strength to reduce the three-dimensional problem of deforming lithosphere to two dimensions, where the horizontal velocity components do not depend on the depth. The components of the momentum equation are vertically integrated using 1-km steps at each of seven Gauss integration points in each finite element (continuum or fault) and the horizontal components of velocity predicted. The vertical component of the momentum equation comes from the assumption of isostatic equilibrium (Bird 1989). The model is composed of two layers with variable thicknesses, plus the topography. Temperature, strength, and the shear stress tensor are depth dependent. By integrating the shear stress along z the problem is reduced to the plane strain. By computing the corresponding strain solution using only the in-plane terms makes the problem bidimensional. SHELLS solves the momentum equation in two dimensions, and the normal vertical stress, assumed as lithostatic, is then added to the result.

The rheology has the same analytical form at all points of the model. The code neglects all elastic strain accumulation and release and solves for velocities, fault slip rates, and anelastic

strain rates and stresses. Deformation occurs by frictional sliding or nonlinear dislocation creep. Given a strain rate, the deviatoric stress is evaluated separately for each of three flow laws: frictional faulting, dislocation creep (power law), and Newtonian creep (linear). At each point, the flow law that provides the lowest maximum shear stress is selected. The rheological parameters are different for the crust and mantle lithosphere. The rheological parameters impose the lithospheric rigidity and the coupling between the crust and the lithospheric mantle. The chosen parameters represent an average lithosphere. Frictional faulting stress is evaluated under the assumption of hydrostatic pore pressure. Faults are distinguished from continuum elements because of double "slipping" nodes, and a lower frictional coefficient with respect to the continuum medium.

The method incorporates some 3-D characteristics since volume integrals of density and strength are performed numerically in a lithosphere model with laterally varying crust and mantle-lithosphere layer thicknesses, heat flow, and elevation. Crustal and lithospheric mantle structure, and steady state thermal regime have been derived from literature data.

References

2007 WGCEP (Working Group on California Earthquake Probabilities) (2008) The uniform California earthquake rupture forecast, version 2 (UCERF 2). USGS Open File Report 2007-1437, U.S. Geological Survey, Reston, Virginia, 104 pp

Albarello D, Mucciarelli M (2002) Seismic hazard estimates using ill-defined macroseismic data at site. Pure Appl Geophys 159:1289–1304

Altamimi Z, Sillard P, Boucher C (2002) ITRF2000: a new release of the International Terrestrial Reference Frame for earth science applications. J Geophys Res 107(B10):2214. doi:10.1029/2001JB000561

Barba S (2007) Numerical modelling of strain rates in Italy. IUGG Perugia, Abstract 11886

Barba S, Carafa MMC, Boschi E (2008) Experimental evidence for mantle drag in the Mediterranean. Geophys Res Lett 35: doi:10.1029/2008GL033281

Barba S, Carafa MMC, Mariucci MT, Montone P, Pierdominici S (2009) Active stress field modelling in the southern Apennines (Italy) using new borehole data. Submitted to Tectonophysics

Basili R, Valensise G, Vannoli P, Burrato P, Fracassi U, Mariano S, Tiberti MM (2008) The database of individual seismogenic sources (DISS), version 3: summarizing 20 years of research on Italy's earthquake geology. Tectonophysics 453:20–43 doi:10.1016/j.tecto.2007.04.014

Bird P (1989) New finite element techniques for modeling deformation histories of continents with stratified temperature-dependent rheology. J Geophys Res 94:3967–3990

Bird P (1999) Thin-plate and thin-shell finite-element programs for forward dynamic modeling of plate deformation and faulting. Comput Geosci 25(3):383–394

Bressan, Bragato (2009) Seismic deformation pattern in the Friuli–Venezia Giulia region (north-eastern Italy) and western Slovenia. Boll Geof Teor Appl 50:255–275

Caporali A (2007) Geophysical characterization of the main seismogenic structures. In Final Reports of the Project "Assessing the Seismogenic Potential and the Probability of Strong Earthquakes in Italy," edited by D. Slejko and G. Valensise, pp. 25–42, Ist. Naz. di Geofis. e Vulcanol., Rome (available at http://hdl.handle.net/2122/3090)

Caporali A, Martin S, Massironi M (2003) Average strain rate in the Italian crust inferred from a permanent GPS network. Part 2: strain rate vs. seismicity and structural geology. Geophys J Int 155:254–268

Caporali A, Aichhorn C, Becker M, Fejes I, Gerhatova L, Ghitau L, Grenerczy Gy, Hefty J, Krauss S, Medak D, Milev G, Mojzes M, Mulic M, Nardo A, Pesec P, Rus T, Simek J, Sledzinski J, Solaric M, Stangl G, Vespe F, Virag G, Vodopivec F, Zablotskyi F (2008) Geokinematics of Central Europe: new insights from the CERGOP-2/Environment Project, J. of Geodynamics (accepted manuscript)

Frankel A, Mueller C, Harmsen S, Wesson R, Leyendecker E, Klein F, Barnhard T, Perkins D, Dickman N, Hanson S, Hopper M (2000) USGS National Seismic Hazard Maps. Earthq Spectra 16:1–20

Gruppo di lavoro CPTI (2004) Catalogo Parametrico dei Terremoti Italiani, versione 2004 (CPTI04). INGV, Bologna. http://emidius.mi.ingv.it/CPTI04/

Hanks TC, Kanamori H (1979) A moment magnitude scale. J Geoph Res 84:2348–2350

Kong X, Bird P (1995) Shells: a thin-plate program for modeling neotectonics of regional or global lithosphere with faults. J Geophys Res 100:22129–22131

Kostrov VV (1974) Seismic moment and energy of earthquakes, and seismic flow of rock. Izv Earth Physics English Transl 1:13–21

Montone P, Mariucci MT, Pondrelli S, Amato A (2004) An improved stress map for Italy and surrounding regions (central Mediterranean). J Geophys Res 109:B10410 doi:10.1029/2003JB002703

Peruzza L (2006) Earthquake probabilities and probabilistic shaking in Italy in 50 years since 2003: trials and ideas for the 3rd generation of Italian seismic hazard maps. Boll Geof Teor Appl 47:515–548

Peruzza L, Pace B, Cavallini F (2009) Error propagation in time-dependent probability of occurrence for characteristic earthquakes in Italy. J Seismol

Press WH, Teukolsky SA, Vetterling WT, Flannery BP (1992) Numerical recipes in Fortran—the art of scien-

tific computing, 2nd edn. Cambridge University Press, Cambridge, 963 pp
Savage JC, Simpson RW (1997) Surface strain accumulation and seismic moment tensor. Bull Seism Soc Am 87:1345–1353
Schwartz DP, Coppersmith KJ (1984) Fault behavior and characteristic earthquakes: examples from the Wasatch and San Andreas fault zones. J Geophys Res 89:5681–5698
Serpelloni E, Anzidei M, Baldi P, Casula G, Galvani A, Pesci A, Riguzzi F (2002) Combination of permanent and non permanent GPS networks for the evaluation of the strain rate field in the Central Mediterranean area. Boll Geofis Teor Appl 43(3/4):195–219
Serpelloni E, Vannucci G, Pondrelli S, Argnani A, Casula G, Anzidei M, Baldi P, Gasperini P (2007) Kinematics of the Western Africa-Eurasia plate boundary from focal mechanisms and GPS data. Geophys J Int 169(2):1180–1200
Stirling MW, Wesnousky SG, Berryman KR (1998) Probabilistic seismic hazard analysis of New Zealand. N Z J Geol Geophys 41:355–375
Stirling MW, Peruzza L, Slejko D, Pace B (2007) Seismotectonic modelling in northeastern Italy. GNS Science Consultancy Report 2007/84, GNS Science, Wellington, 22 pp
Ward SN (1994) A multidisciplinary approach to seismic hazard in southern California. Bull Seism Soc Am 84:1293–1309
Ward SN (1998) On the consistency of earthquake moment rates, geological fault data, and space geodetic strain: the United States. Geoph J Int 134:172–186
Ward SN (2007) Methods for evaluating earthquake potential and likelihood in and around California. Seismol Res Lett 78:121–133
Weichert (1980) Estimation of the earthquake recurrence parameters for unequal observation periods for different magnitudes. Bull Seism Soc Am 70:1337–1346
Wells DL, Coppersmith KJ (1994) New empirical relationship among magnitude, rupture length, rupture width, rupture area, and surface displacement. Bull Seism Soc Am 84:974–1002
Wessel P, Smith W (1991) Free software helps map and display data. EOS Trans AGU 72:441–461
WGCEP (Working Group on California Earthquake Probabilities) (1995) Seismic hazards in southern California: probable earthquakes, 1994 to 2024. Bull Seism Soc Am 85:379–439
WGCEP (Working Group on California Earthquake Probabilities) (2003) Earthquake probabilities in the San Francisco Bay Region: 2002–2031. U.S. Geol. Surv. Open-File Report 03-214, 234 pp